ARTICLE

Received 00th January 20xx,
Accepted 00th January 20xx

DOI: 10.1039/x0xx00000x

Phase evolution, speciation and solubility limit of aluminium doping in zinc oxide catalyst supports synthesized via co-precipitated hydrozincite precursors

Benjamin Mockenhaupt [#ab], Jan Konrad Wied[#c], Sebastian Mangelsen[b], Ulrich Schürmann[d], Lorenz Kienle[d], Jörn Schmedt auf der Günne [*c] and Malte Behrens [*ab]

[a.] *Institute of Inorganic Chemistry, University of Duisburg-Essen, Universitätsstr. 7, 45141 Essen (Germany), E-Mail: mbehrens@ac.uni-kiel.de.*
[b.] *Institute of Inorganic Chemistry, Kiel University, Max-Eyth-Str. 2, 24118 Kiel (Germany).*
[c.] *Institute of Inorganic Chemistry, University of Siegen, Adolf-Reichwein-Straße 2, 57076 Siegen (Germany), E-Mail: gunnej@chemie.uni-siegen.de.*
[d.] *Department of Material Science, Kiel University, Kaiserstraße 2, 24143 Kiel (Germany).*

[#] *Both authors contributed equally.*
[*] *Corresponding authors.*

Electronic Supplementary Information (ESI) available: [details of any supplementary information available should be included here]. See DOI: 10.1039/x0xx00000x

Supporting Information

Description of the crystal structure of hydrozincite

The layered structure of hydrozincite (see Fig. S1) consists of layers made up of edge-sharing Zn-O octahedra with ordered voids. Above and below these voids, additional Zn^{2+} resides in tetrahedral coordination, where the CO_3^{2-} anion connects the tips of the tetrahedra with octahedra of the adjacent layer. A detailed description of the hydrozincite structure was reported by *Ghose et al.* [1].

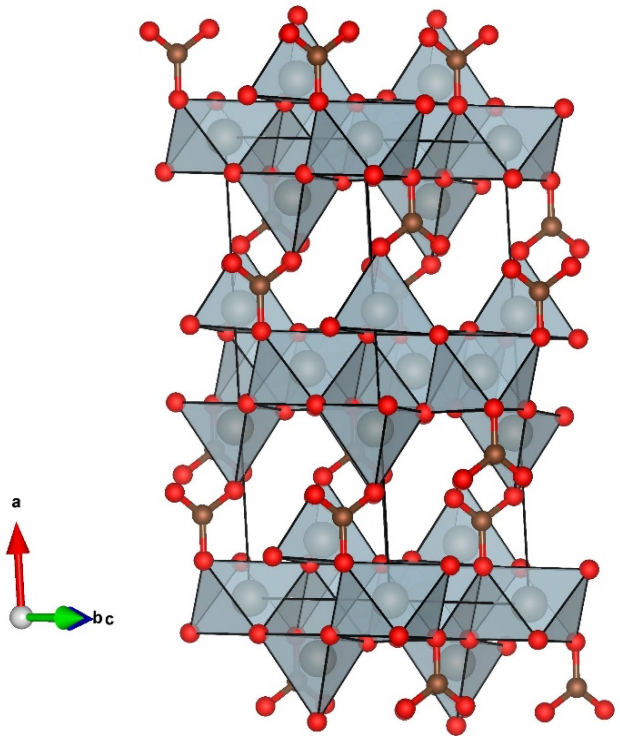

Figure S1 Crystal structure of hydrozincite with viewing direction parallel to the layers.[1] Color code: red: oxygen, brown: carbon, grey: zinc.[2]

Materials used for co-precipitation

Table S1 List of the used metal salts and their purities for co-precipitation.

Chemicals	Supplier	Purity
$Zn(NO_3)_2 \cdot 6\ H_2O$	Carl Roth GmbH + Co. KG	≥ 99 %
$Al(NO_3)_3 \cdot 9\ H_2O$	Carl Roth GmbH + Co. KG	≥ 98 %

Time resolved ageing of x_{Al} = 0.02 Al doped hydrozincite

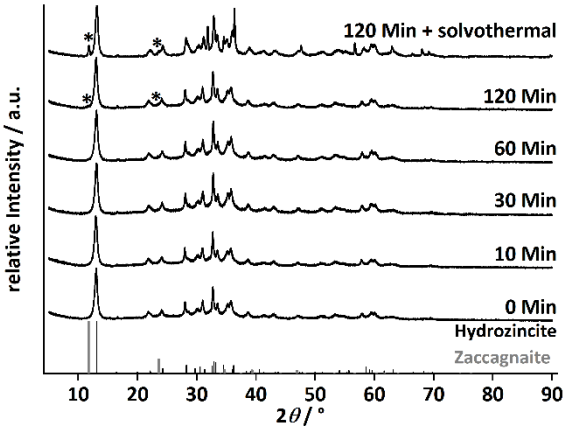

Figure S2 XRPD data of the time resolved ageing of aluminium doped hydrozincite for x_{Al} = 0.02. The ageing was performed from 0 min (immediately after precipitation) to 120 min in the precipitation reactor. The residue after 120 minutes ageing time was treated solvothermal at 130 °C. The black bars correspond to the ICSD reference of hydrozincite (#16583) and the grey bars correspond to the ICSD reference of the zaccagnaite side phase (#190041), whose main reflections are marked with a star.

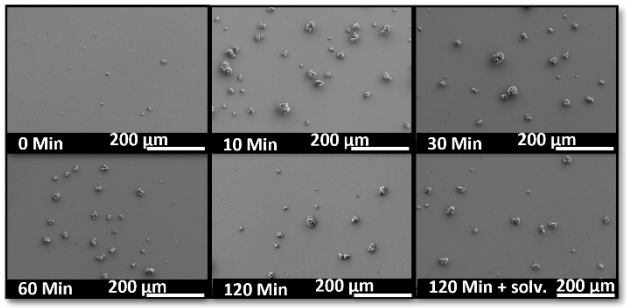

Figure S3 Overview SEM images of the time resolved ageing experiment with an aluminium incorporation of x_{Al} = 0.02 into the precursor phase. The times indicate after which ageing time the sample was taken out of the synthesis reactor. After 120 minutes ageing, the suspension was treated at 130 °C for additional 12 hours in a solvothermal reactor with Teflon liner (picture on the bottom, right, 120 Min + solv.).

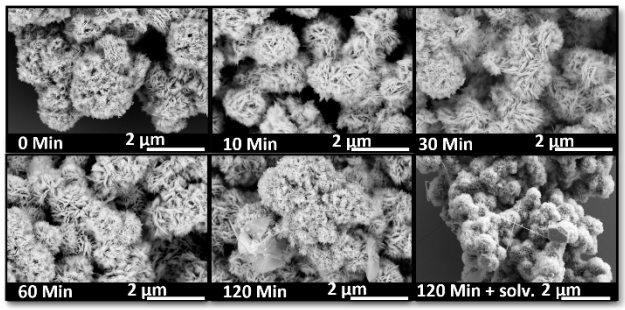

Figure S4 SEM micrographs of the ZnO:Al synthesized from the precipitates after co-precipitation of a zinc-aluminium solution with an aluminium content of x_{Al} = 0.02 and different ageing times. After 120 minutes ageing, the solution was treated at 130 °C for additional 12 hours in a solvothermal reactor with Teflon liner (picture on the bottom, right, 120 Min + solv.). Calcination was performed at 320 °C with a heating ramp of 2 °C min^{-1} for 4 h in static air.

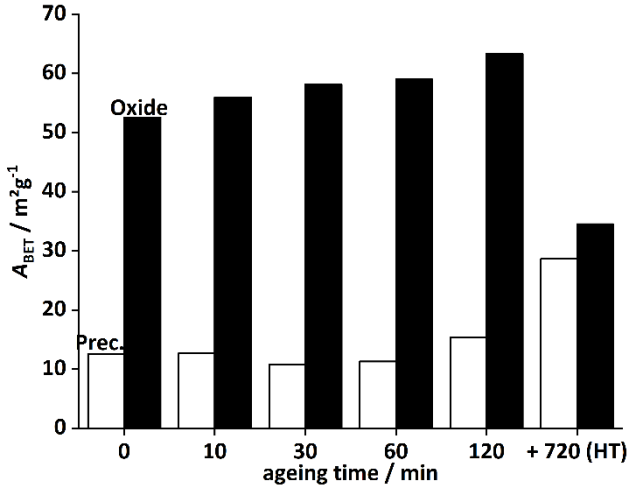

Figure S5 Evolution of the specific surface area as function of ageing time of the co-precipitated aluminium doped hydrozincites (Prec.) and their corresponding zinc oxides (Oxide). The precipitation was carried out with a zinc-aluminium solution, containing an aluminium amount of x_{Al} = 0.02. After 120 minutes ageing time the suspension was aged for additional 12 hours in a hydrothermal reactor with Teflon liner at 130 °C (+720 (HT)).

The morphology of the hydrozincite powders with x_{Al} = 0.02 aluminium incorporation aged for different temperatures is shown in Fig. S3 and Fig. S4. The SEM images show that in the first 10 minutes ageing time the aggregates grew and almost reached their final size (Fig. S3). A closer look into the particle morphology, shown in Fig. S4, demonstrates the change in morphology in dependency of the ageing time. After co-precipitation, the aggregates are formed by small platelets. After 10 minutes, the platelet structure is more clearly present. At 120 minutes, larger additional platelets are observed and aligned to the hydrotalcite side phase (zaccagnaite), as discussed in the main text. From this observation it can be concluded that the aluminium favours an incorporation into a hydrotalcite side phase. The Al enrichment in a hydrotalcite side phase could be thermodynamically favoured, that is why the side phase evolved after 120 minutes ageing time and increased in the solvothermal ageing step. These additional platelets grew out of the aggregates. At the same time, the morphology of the bulk structure was changed to smaller platelets. The further treatment at 130 °C in a solvothermal reactor resulted in an enhanced grow of the larger platelets, which were afterwards substantially thicker. Simultaneously, rods are also formed and present besides the typical aggregates as observed after 10 minutes ageing time.

Simultaneously to the larger platelets, the specific surface area of the precipitate as determined by nitrogen physisorption increased (Fig. S5).

Synthesis of the aluminium-rich side-phase zaccagnaite

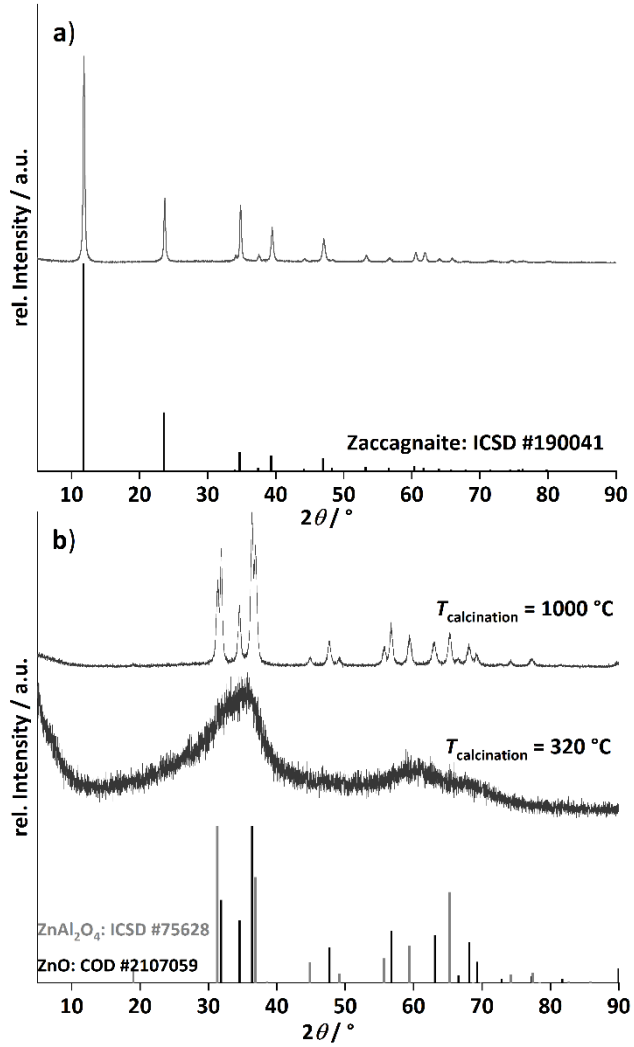

Figure S6 Powder XRD data of the co-precipitated zaccagnaite precursor a) with reference from ICSD (#190041) and the calcined samples at different temperatures b) with reference for ZnO from COD (#2107059, black, broad bars) and zinc-aluminium spinel from ICSD (#75628, grey bars).

The aluminium-rich side-phase zaccagnaite synthesized as a reference material should nominally contain 33% of aluminium (metal based). The precipitation was carried out in an automated stirred tank reactor (OptiMax, Mettler Toledo) from 0.4 M metal salt nitrate solution at a temperature of 50 °C and at a constant *pH* of 8.5. As precipitating agent, 0.09 M sodium carbonate together with 0.6 M sodium hydroxide solution were used. The dosing rate of metal solution was adjusted to 2.08 g min^{-1}. After precipitation the precipitate was aged for 60 minutes without further *pH* control in the mother liquor. The precursor was washed with deionized water 10 times, to reach a conductivity of the wastewater lower than 100 µS cm^{-1} and dried at 80 °C for minimum 14 hours.
The PXRD characterization of the phase pure precursor and the calcined sample is shown in Fig. S6. Calcination at 320 °C resulted in an amorphous solid. The position of the evolved broad halo between $2\theta = 30 - 40$ ° is in a range where ZnO as well as the spinel exhibit strong reflections. After calcination at 1000 °C, ZnO as well as the spinel crystallized and segregated. The reflections are quite sharp and small, indicating macroscopic crystallites.

Beam damage of the prepared zaccagnaite reference material in TEM-investigations

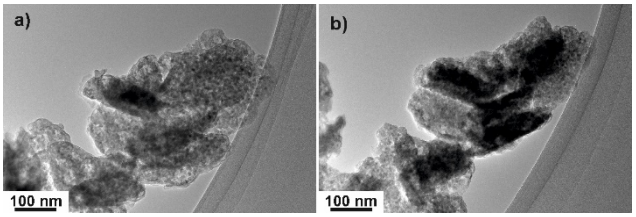

Figure S7 Demonstration of the morphology changes during electron beam exposure of the prepared zaccagnaite in the TEM: a) shows the pristine material while figure b) was recorded after a beam exposition of some minutes including electron diffraction and EDX analysis. The measurement was performed at room temperature.

In Fig. S7 the morphology change of the zaccagnaite material during TEM-analysis is shown. The measurement was performed at room temperature. From TG-analysis of that material, shown in Fig. S13, the material decomposes at around 150 °C, which is a quite low temperature. Because of the high vacuum and the radiation energy input at TEM-investigations, an earlier decomposition may happen. Therefore, a degradation of the material cannot easily prevent and takes place, as it was observed in a loss of oxygen determined by EDX, which is associated with the emission of the decomposition products H_2O and CO_2. Such change in chemical composition as a result of beam exposure is known and also found in investigations of nickel-iron layered double hydroxides. [3, 4] From the finding it was assumed that the zaccagnaite sample decomposed into defect enriched zinc oxide, as the d-values determined by electron diffraction are in the range of ZnO but with a deviation up to 5%. This result correlates to the reported investigation on nickel-iron layered double hydroxides. [3]

To demonstrate the origin of the defect enriched ZnO that originates form thermal decomposition of zaccagnaite, *in situ* PXRD analysis of the calcination was performed. The decomposition starts with a pronounced shift of the *00l* reflections at around 150 °C as shown in Fig. S8, which is assigned to the loss of inter-layer water and the resulting contraction of the inter-layer distances. A slow crystallization of ZnO was observed by a monotonic change of the PXRD patterns with further increasing temperature. Only above 550 °C, the main reflections of the ZnO became clearly visible. These results support the suggestion that the beam-damaged state and the state after mild thermal decomposition are similar. Furthermore, they provide support for the assumption that the defect enriched ZnO with oriented domains found in the calcined samples, shown in the main text in Fig. 11 and Fig. 12, have their origin in the decomposed hydrotalcite-structure of zaccagnaite.

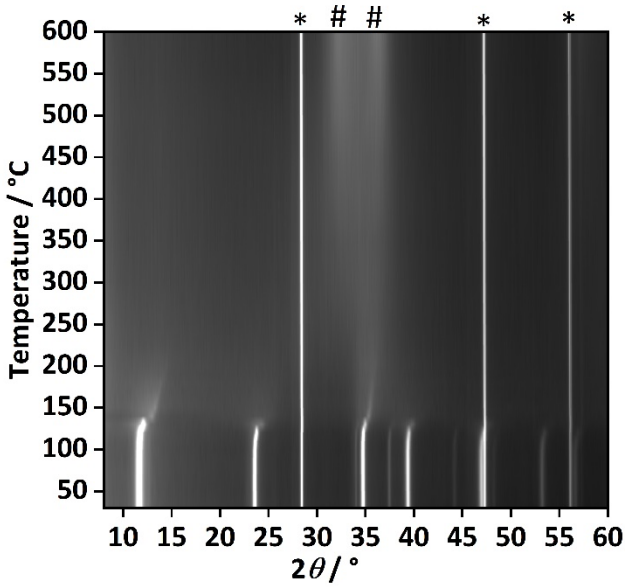

Figure S8 Temperature resolved PXRD analysis of the decomposition of the Zaccagnaite precursor. The PXRD analysis was performed with silicon as standard and in static air. Reflections of Si (*) and ZnO (#) are indicated by labels.

Characterization of the hydrozincite precursors of the aluminium concentration variation

Powder XRD and SEM analysis

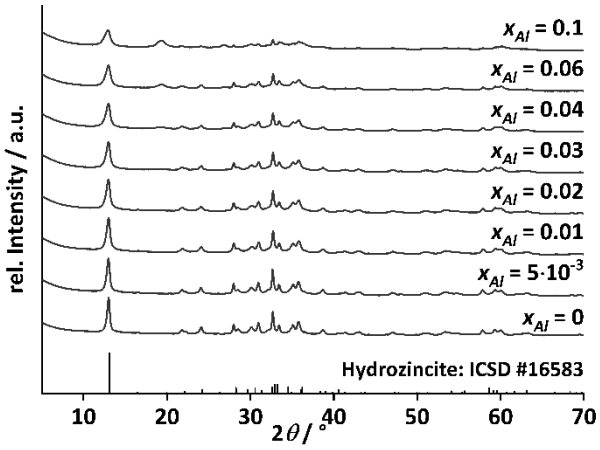

Figure S9 PXRD data of the co-precipitated aluminium doped hydrozincite precursors Al:$Zn_5(OH)_6(CO_3)_2$. x_{Al} is the metal based aluminium ratio. The black bars correspond to the reference of hydrozincite (ICSD#16583).

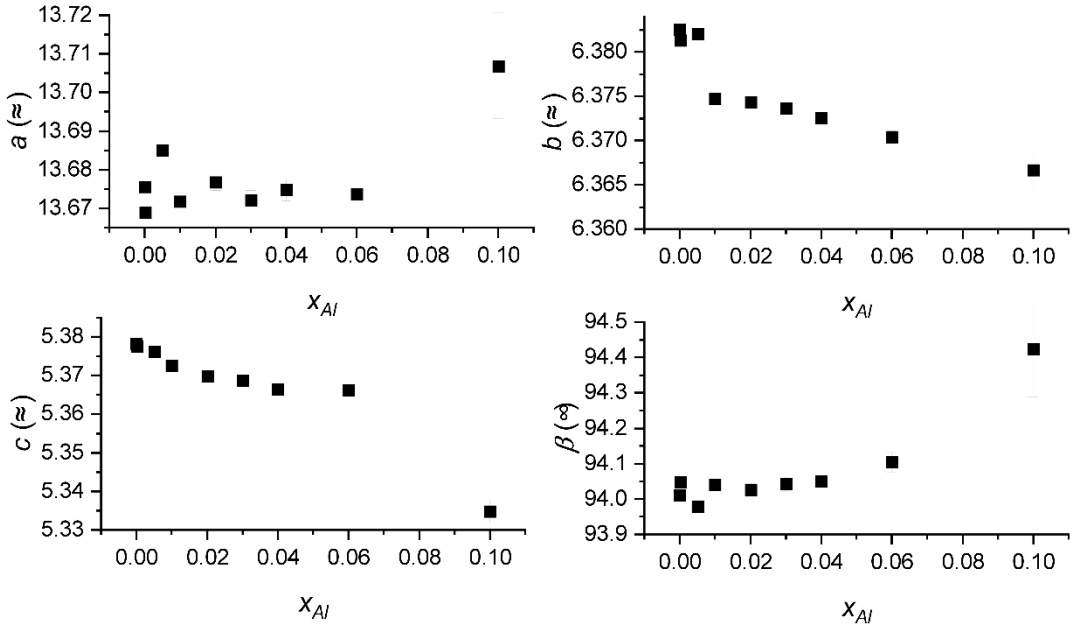

Figure S10 Lattice parameter of the refined PXRD pattern of the aluminium doped hydrozincites in dependency of the aluminium content.

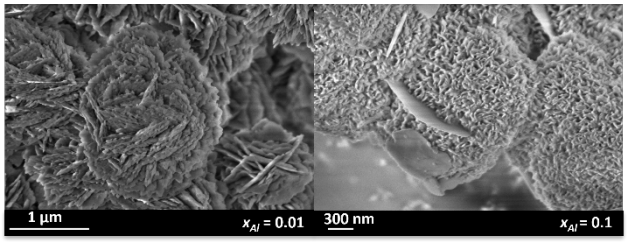

Figure S11 Morphology comparison in dependency of the aluminium content in aluminium-doped hydrozincites Al:$Zn_5(OH)_6(CO_3)_2$ after co-precipitation and drying. The larger hexagonal platelets are assigned to the aluminium-rich side-phase zaccagnaite (see main text for details).

The influence of the aluminium doping on the particle morphology was determined by SEM analysis of the hydrozincite with x_{Al} = 0.01 (Fig. S11 left side) and x_{Al} = 0.1 (Fig. S11 right side) aluminium content. For low doping amounts, inter-grown platelets that form spherical aggregates were observed. The doping with x_{Al} = 0.1 aluminium content resulted also in spherical aggregates, but they were built up of much smaller primary particles of a platelet shape. Simultaneously the morphology is no longer uniform. Large hexagonal platelets (compare Fig. S11 right image) are present in addition. These platelets are aluminium enriched, which

was confirmed by EDX analysis (compare Fig. S12) as listed in Table S2. The higher doping level resulted into inhomogeneous distributed aluminium in the precursor material due to the segregation of this aluminium-rich side-phase, which was identified as zaccagnaite (see main text for details). This result was also found in the hydrozincite sample with x_{Al} = 0.03, where also a hydrotalcite signal was present in the corresponding PXRD pattern (Fig. 3 b)).

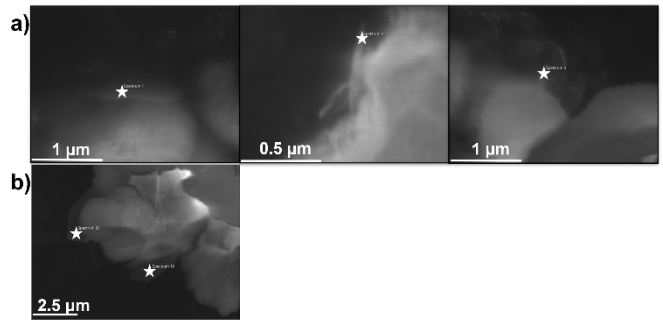

Figure S12 SEM images of the recorded EDX point spectra of the large hexagonal platelets, from left Spectrum 1, Spectrum2 and Spectrum 3 the analysed spot is marked with a star. The pictures of a) contained to hydrozincite doped with xAl = 0.1 aluminium. The pictures of b) contained to hydrozincite with xAl = 0.03 aluminium amount (Spectrum19 (left) and Spectrum 20 (right)).

Table S2 Aluminium and zinc ratio of the analysed platelets by SEM-EDX, shown in Figure S12.

# Spectrum	Zn / at.-%	Al / at.-%	$x_{Al/(Zn+Al)}$	$M^{2+}:M^{3+}$
1	70	30	0.3	2
2	74	26	0.3	3
3	72	28	0.3	3
19	92	8	0.1	12
20	81	19	0.2	4

Thermogravimetric analysis of the precursor samples

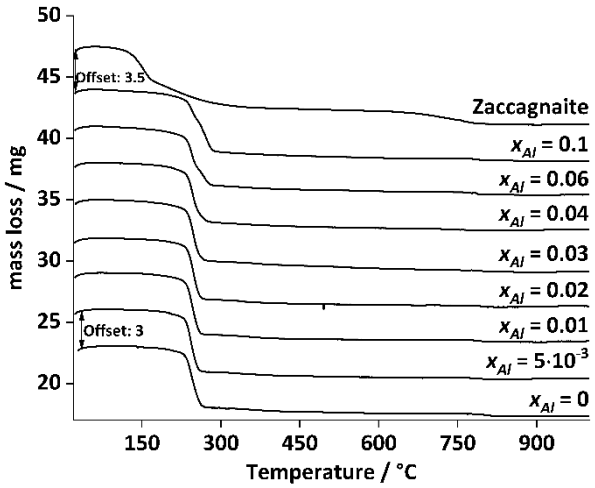

Figure S13 Thermogravimetric analysis of the decomposition of the hydrozincite precursors in synthetic air with heating ramp of 6 °C min^{-1} up to 1000 °C. x_{Al} is the metal-based fraction.

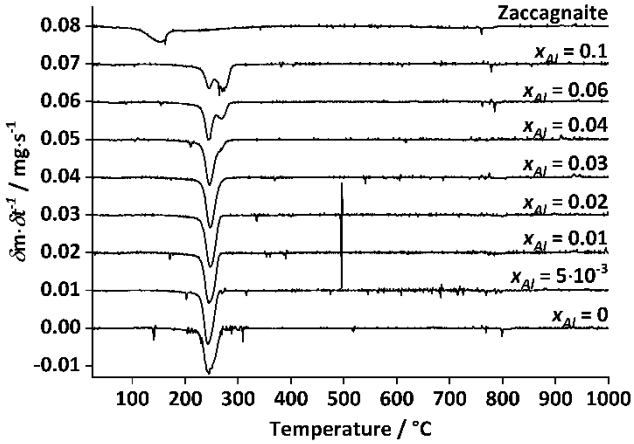

Figure S14 Differential thermogravimetric analysis of the decomposition of the hydrozincite precursors in synthetic air with heating ramp of 6 °C min^{-1} up to 1000 °C. x_{Al} is the metal-based fraction.

The decomposition of the co-precipitated hydrozincites and of the zaccagnaite reference compound were analysed by thermogravimetric measurements on a STA 1600 from Linseis (shown in Fig. S13 and Fig. S14) in synthetic air heating the sample from room temperature to 1000 °C with a heating ramp of 6 °C min^{-1}. The hydrozincites start to decompose at around 220 °C and the decomposition process is completed at 300 °C. Therefore, the calcination temperature of 320 °C is high enough to ensure complete transformation but is low enough to create high-surface area materials and to prevent sinter effects. At x_{Al} = 0.04 and higher aluminium contents, the DTG signal shows a shoulder or second event at higher temperatures indicating an additional phase beside the hydrozincite. Because of the presence of the zaccagnaite side phase in this samples, found by PXRD analysis, the two decomposition steps could be assigned to the separated decomposition of hydrozincite and hydrotalcite. However, the zaccagnaite reference was found to decompose at lower temperature.

Infrared analysis

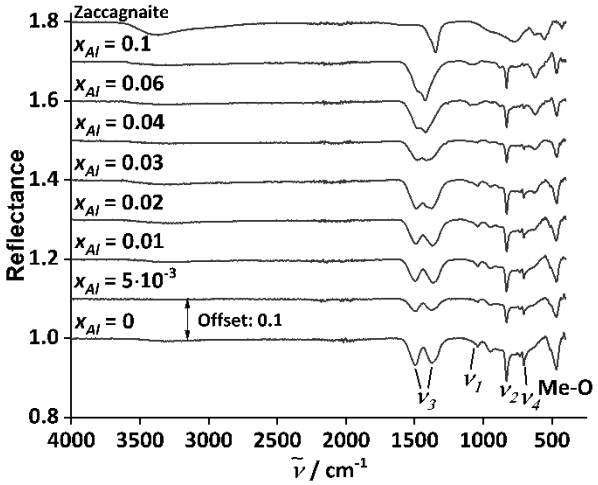

Figure S15 Complete range infrared spectroscopy of the aluminium doped hydrozincites Al:$Zn_5(OH)_6(CO_3)_2$ in comparation with the aluminium rich hydrotalcite side phase zaccagnaite. x_{Al} is the metal-based fraction of aluminium.

In Fig. S15 the stack plot of the measured infrared spectra of the aluminium doped hydrozincite samples are shown. The main text provides a brief discussion on the changes in the spectra observed with varying aluminium content. Here, the general assignment of the bands and further details are discussed.

In the range of 3600 cm^{-1} to 3200 cm^{-1} the stretching band of OH^- ions should be detectable, which hints to stacking disorders. [5] In our synthesis series only one broad weak absorption band around 3300 cm^{-1} was detected (Fig. S16). This band is originated by the hydrogen bond between a hydroxyl-group and an oxygen of a carbonate ion as well as by the stretching mode of the hydroxide groups. [6] In contrast, this mode is more pronounced in the hydrotalcite reference material, caused by the higher amount of hydroxide groups. [7]

The ν_3 modes of the hydrozincite broaden as more aluminium was incorporated. Simultaneous a shift of the ν_3 absorption peak from ≈1370 cm^{-1} (x_{Al} = 0) to a higher wavenumber 1422 cm^{-1} (x_{Al} = 0.1) was induced. The mode at around 1490 cm^{-1} did not shift.

The ν_1 mode showed a similar behaviour. This absorption became weaker and simultaneous a shift towards higher wavenumbers can be observed (1041 cm^{-1} to 1081 cm^{-1}). In contrast to this observation, the ν_4 modes became only weaker and did not shift. The signal of the out-of-plane OCO bending mode (ν_2) was in all hydrozincite samples present without shifting, but a second ν_2 mode appeared for higher aluminium content samples. Typically, an LDH phase contains only one ν_3 absorption mode [7-9]. The hydrozincites with x_{Al} = 0.06 and x_{Al} = 0.1 aluminium content seem to change in the ν_3 absorption modes towards a hydrotalcite like signal.

The infrared mode at 621 cm^{-1} appeared for $x_{Al} > 0.01$ and increased with the aluminium content. From hydrotalcite-like materials with different divalent cations, the mode in this region was found to be induced by translation of the hydroxyl groups between the sheets. [7] The increase in the absorption band in the hydrozincite samples is larger than the mode in the aluminium rich Zaccagnaite sample. Therefore, this mode corresponds more probably to the Zn-OH and to the Al-OH in the hydrozincite, which simultaneously explains the broadening with increasing aluminium content. An increase in the translation mode of hydroxyl-groups does indicate that the amount increased. Therefore, the possibility of an increased number of sheets is given and demonstrates the sublattice change as an incorporated additional charge. An increased number of sheets will result in more but smaller primary particles and in increased defect sites of the host lattice.

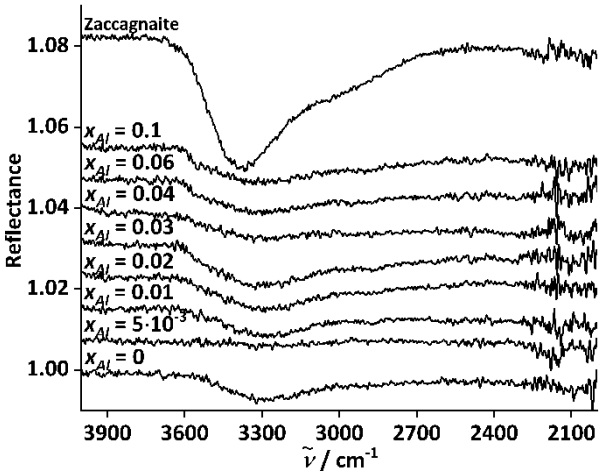

Figure S16 Focused infrared spectra of the aluminium doped hydrozincites Al:$Zn_5(OH)_6(CO_3)_2$ in comparation with the aluminium rich hydrotalcite side phase to demonstrate the OH^- stretching mode (around 3300 cm^{-1}).

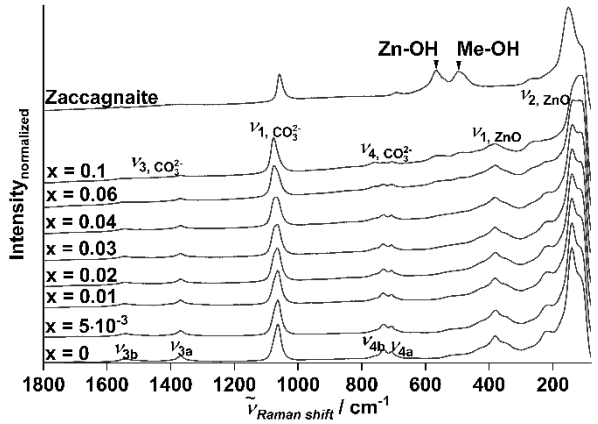

Figure S17 Raman spectra of the aluminium doped hydrozincites Al:$Zn_5(OH)_6(CO_3)_2$ in comparation with the aluminium rich hydrotalcite side phase.

Characterization of the zinc oxides

Elemental composition and nitrogen physisorption

0The metal amount was determined with an Avio 200 ICP Optical Emission Spectrometer with a PerkinElmer S23 Autosampler. Before analysis, 5 mg of the metal oxide was dissolved in nitric acid. In Fig. S18 the measured aluminium ratios in comparison with the nominal ratios are plotted. The targeted ratio was reached for samples with lower aluminium content than 6%. For higher aluminium contents (x_{Al} > 4%) the deviation of the measured composition from the nominal targeted composition was larger.

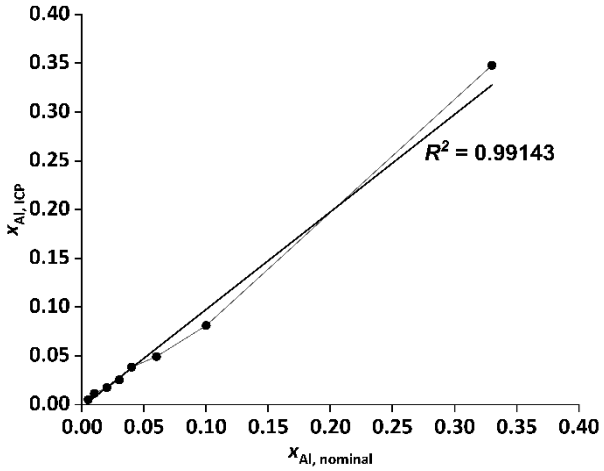

Figure S18 Metal based aluminium content determined by ICP analysis of the oxides. The line between the datapoints if to guide the eye.

Elemental composition and pore size distribution and pore volume

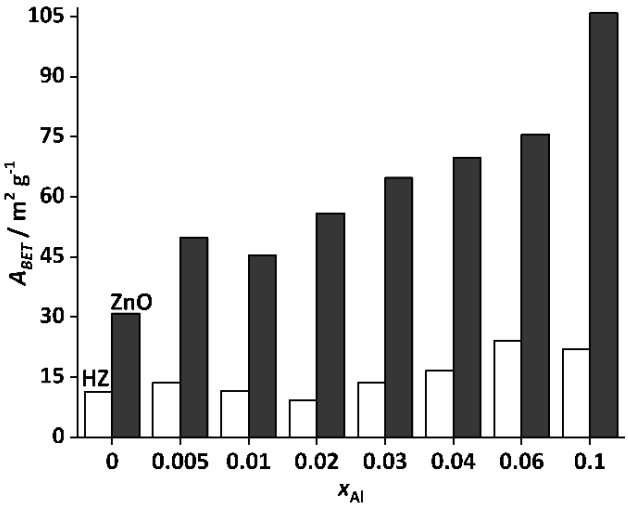

Figure S19 BET-surface area evolution of aluminium doped hydrozincites (HZ: hydrozincite precursors) and the resulting zinc oxides (ZnO) after calcination at 320 °C for 4 h in static air. x_{Al} indicated the cation-based molar aluminium fraction.

ARTICLE

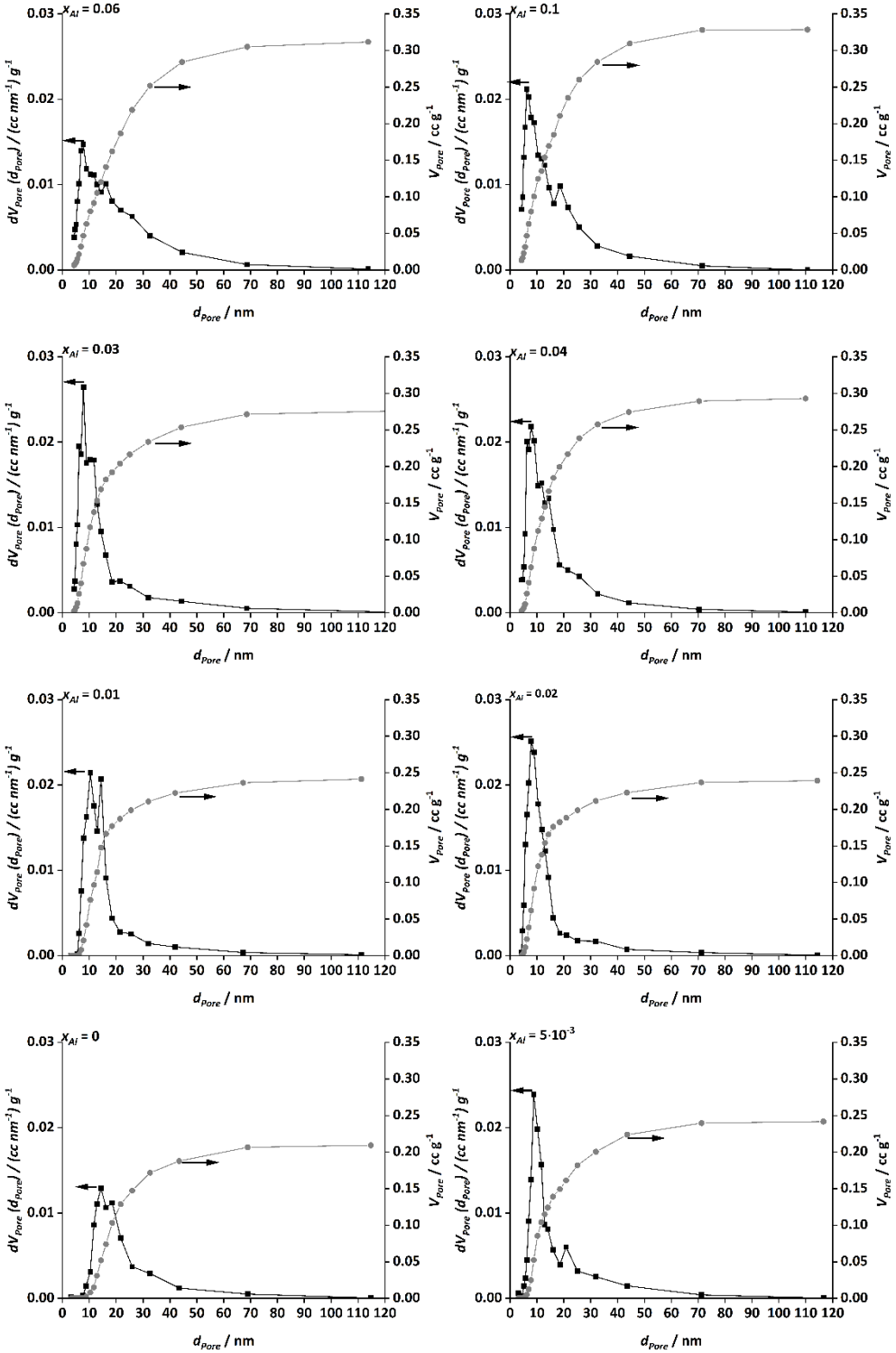

Figure S20 Pore size and -volume distribution of the aluminium doped zinc oxide series. x_{Al} is the metal-based fraction of Al. The lines are to guide the eye.

ARTICLE

Raman spectroscopy

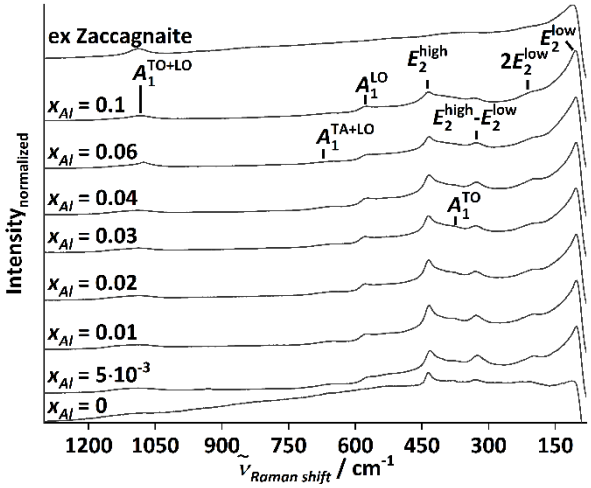

Figure S21 Raman spectra of the aluminium doped zinc oxides in comparation with the aluminium rich hydrotalcite side phase (ex-zaccagnaite). The calcination was performed at 320 °C for 4 h in static air. The modes are labelled with abbreviations for: Longitudinal optical mode (LO), transversal optical mode (TO) and transversal acoustical mode (TA). The Raman spectra were recorded with a wavelength of 785 nm and 90 mW at 45° rotated sample at room temperature.

To determine the influence of the aluminium incorporation onto the zinc oxide, Raman spectra of the doped zinc oxide samples were recorded (compare Fig. S21). The classification of the modes was performed by the description from Arguello *et al.* [10] and Cuscó *et al.* [11] The spectra show the non-polar E_2 and the polar A_1 modes as well as some side modes like the acoustic overtone of the E_2^{low} signed as $2E_2^{low}$. [12] The labelled spectrum "ex Zaccagnaite" is the synthesized reference sample of the side-phase, described above, which was calcined under the same conditions as the hydrozincites. The E_2^{low} mode is a result of the vibration of the zinc ions whereas the E_2^{high} mode is more assigned to the oxygens moving perpendicular to the c-axis. The oxygen dominated A_1 mode shows the movement of the oxygen ions in parallel to the c-axis whereby an oscillating polarization by the zinc ions is induced. [12] This causes splitting into a longitudinal optical (LO) and a transversal optical (TO) mode. [12,13]
Raman spectroscopy should also be sensitive to side phases in a sample. [13] Compared to the aluminium doped zinc oxide samples the undoped sample had a higher intensity at the E_2^{high} (O sublattice) mode than at the E_2^{low} (Zn sublattice) mode, but the positions of the bands are independent of the dopant amount. The ex-zaccagnaite sample was used to verify, at which position a Raman shift can be expected, if this side phase was calcined under the same conditions. Interestingly, only two sharp peaks are visible. One at around 112 cm^{-1} and the second one at around 1085 cm^{-1}. Both peaks are shifted by ca. 5 cm^{-1} towards higher wavenumbers compared to the zinc oxide samples. In case of side-phase formation in the aluminium doped samples, the A_1^{TO+LO} overtone mode appears more pronounced with increasing aluminium content, especially for the sample containing x_{Al} = 0.06 and x_{Al} = 0.1 aluminium. Since this mode was also present in the undoped zinc oxide sample and since this mode is a second order mode, it cannot be related to aluminium substituted zinc sites. [11] However, this overtone can be assigned to the naturally occurring defects in zinc oxide. [14] By increasing the aluminium content, the PXRD pattern have shown that the 002 reflection (*c*-axis) was affected by the incorporation. This finding can be supported by the increase in the A_1^{TO+LO} mode, which involves the c-plane.
The Raman spectrum of the ex-zaccagnaite sample shows only few Raman modes, which correspond to ZnO, but the shift of about 5 cm^{-1} could support a defect-enriched state of this phase, which is present in high inter-dispersion with additional amorphous aluminium-rich material. [15] This finding is in accordance with the results observed by TEM analysis.

TEM-EDX analysis

Position	Zn / %	Al / %
1	69.5	30.5
2	87.8	12.2
3	61.4	38.6
4	95.5	4.5

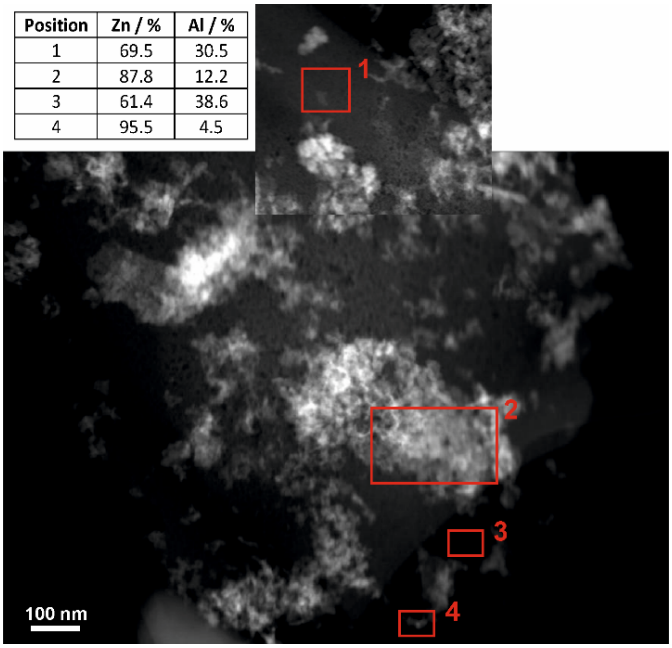

Figure S22 STEM-EDX-analysis of an aluminium doped zinc oxide sample with x_{Al} = 0.03. The windows visualize the analysed regions from which the mean metal-composition was determined, which are shown in the table.

UV/Vis analysis

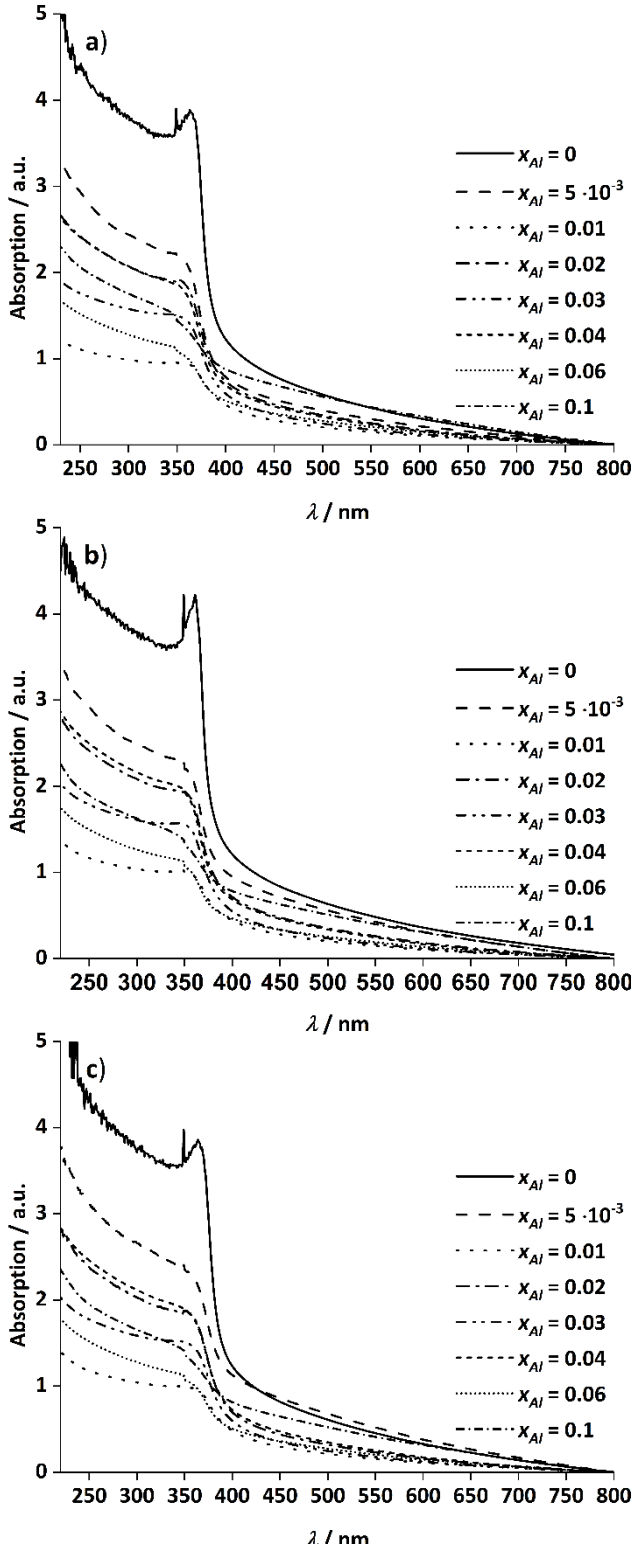

Figure S23 UV-Vis spectra of the aluminium doped zinc oxides. The spectra were recorded at room temperature (a), at -185 °C (b) and at 27 °C (c). The spectra are recorded in transmission geometry and are automatically normalized to 0 for λ = 800 nm.

In Fig. S23 the recorded UV/Vis spectra of the zinc oxide samples are shown. The calcination was performed at 320 °C for each sample. The band gap determination was performed by differentiation of the raw data (Fig. S23), to determine the changing point. This mathematical treatment results in an optimum function, where the minimum corresponds to the changing point. Therefore, the wavelength of this minimum (changing point in Fig. S23) was used to calculate the Band gap energy. Because of the doping effect it is assumed that the absorbance shift towards higher or lower wavelength, as it can be seen by the data in Fig. S23.

However, this shift in absorbance can be followed by the shift of the changing point, which can be mathematically evaluated and reduces evaluation errors. The change of these values with variation of the aluminium doping level is discussed in the main text.

To determine the reliability of the measured data, additional measurements were performed with a UV/Vis spectrometer 2600i of Shimadzu in the range of 200 nm to 900 nm. The sample was pressed into the solid sample holder to create a flat surface. The spectra were recorded in reflection with $BaSO_4$ as reference material. The band gap evaluation was performed as described above. These results are similar to the measurements in transmission mode as it is shown in Fig. S24. To determine the error caused by the preparation method, three additional batches of zinc oxide containing 3 % aluminium (x_{Al} = 0.03) are additionally analysed. These batches correspond to different batches of co-precipitated hydrozincite samples. The results are shown in Table S2. The similar results in band gap energies demonstrate, that the reported data visualize the material properties of the herein reported doping series in a reproducible way.

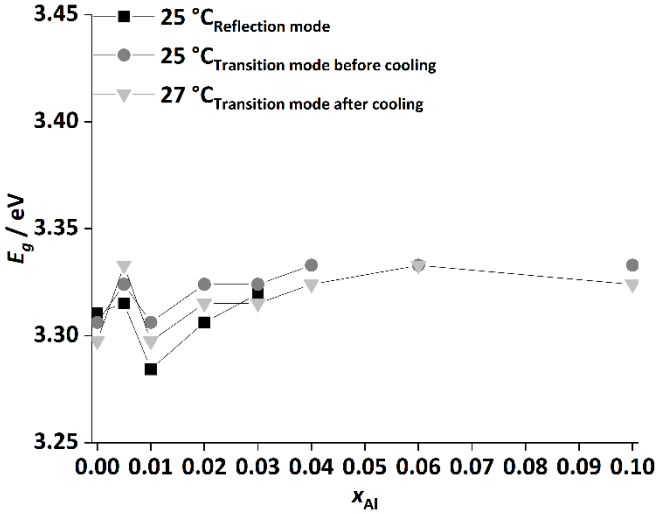

Figure S24 Comparison of the Band gap energies determined in reflection and transmission mode at room temperature.

Table S2 List of the reproduced Band gap measurements of different synthesis batches of ZnO:Al with 3 % Al content (x_{Al} = 0.03).

x_{Al} Synthesis number	E_g / eV measured in reflection mode at 25 °C	E_g / eV measured in transmission mode at 25 °C
0.03-S1	3.32	3.32
0.03-S2	3.32	-
0.03-S3	3.32	-
0.03-S4	3.32	-

High temperature calcination series

Precursor characterization and reference calcination temperature

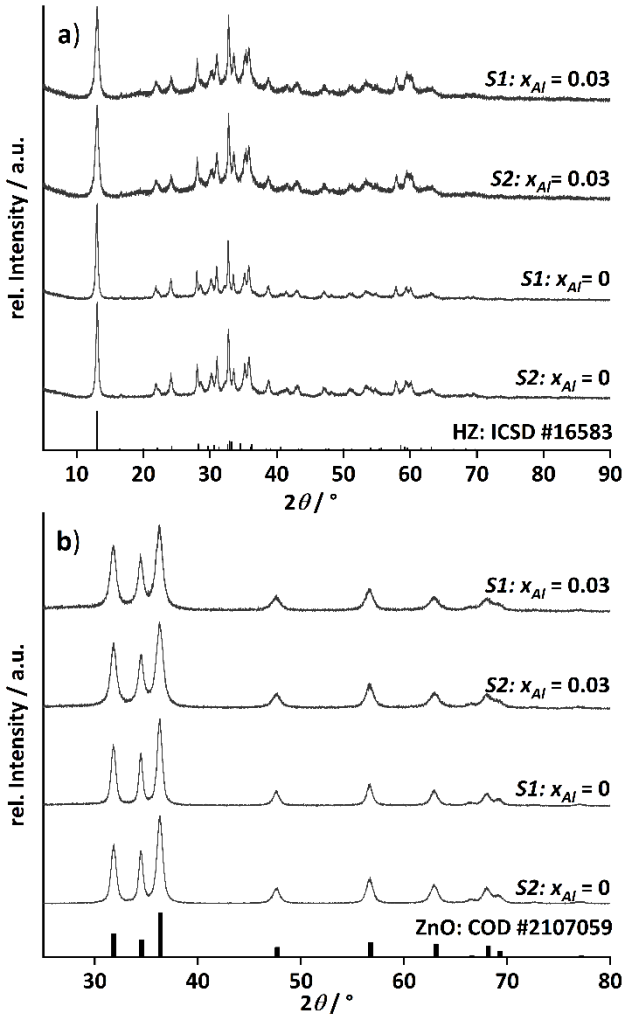

Figure S25 PXRD pattern of the a) precursor (reference from ICSD: 16583, bars) and b) zinc oxide (Reference from COD: 2107059, bars) after calcination at 320 °C of undoped and with 3% aluminium doped samples (x_{Al} = 0.03). The label S1 and S2 are assigned to two different synthesis batches of the same materials. These batches were investigated in the high temperature annealing experiment.

For the comparative high-temperature calcination experiments, the sample with x_{Al} = 0.0 and x_{Al} = 0.03 needed to be reproduced to provide enough material for these investigations. The PXRD pattern of the precursors and of the samples calcined at 320 °C of the new batch S2 and the original batch S1 are compared in Fig. S25 showing that the major sample characteristics could be reproduced and that similar materials have been obtained. The following data has been obtained with the batch S2.

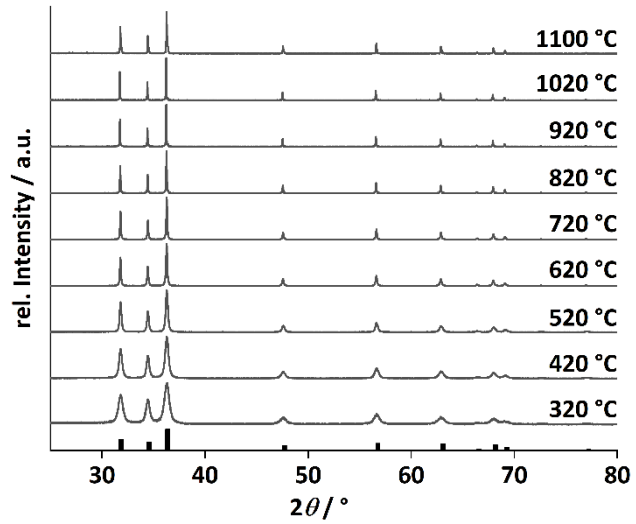

Figure S26 Powder XRD pattern of the undoped zinc oxides after calcination of the hydrozincite precursors at different temperatures with 2 °C min^{-1} heating ramp and 4 h holding time in static air. The reference pattern of zinc oxide (bars) was taken from COD database (#2107059).

For comparison, an undoped zinc oxide was treated in the same way as the 3% aluminium doped zinc oxide (see main text). In Fig. S26 the powder XRD pattern are shown. The reflection width decrease was similar as described for the doped zinc oxide material in the main text, indicating an increased crystallite size, as it was also confirmed by SEM analysis.

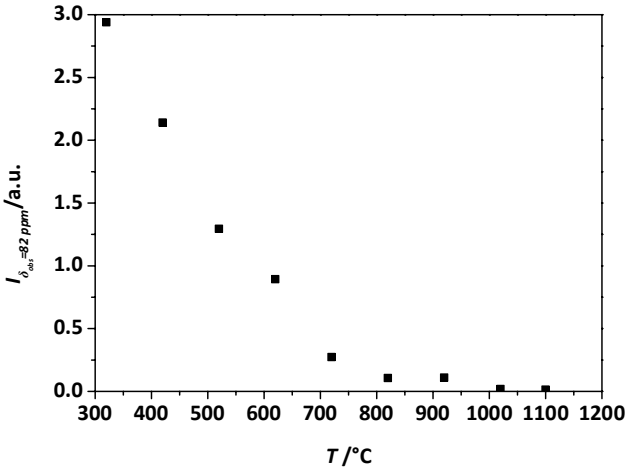

Figure S27 Qualitative change of the ^{27}Al MAS NMR signal at δ_{obs}= 82 ppm of the aluminium enriched zinc oxides, x_{Al} = 0.03, with different annealing temperatures applied. Similar measurement conditions were applied for the individual measurements , i.e. it was assumed that the quadruple parameters do not change while recycle delays were bigger then $3 \cdot T_1$.

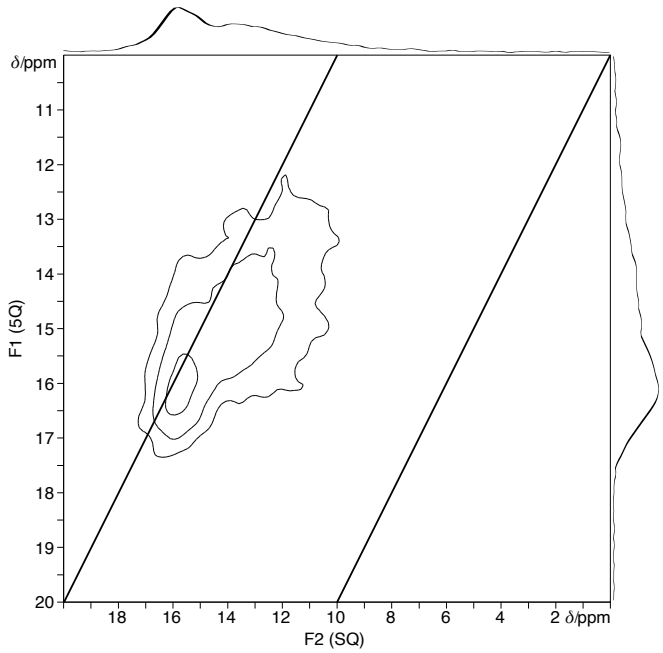

Figure S28 Sheared ^{27}Al 2D quintuple-quantum MQMAS NMR spectrum of zaccagnaite acquired at a spinning frequency of 20 kHz. The acquisition was performed at 20.0 kHz sample spinning frequency using a three-pulse sequence with a zero-quantum filter[16], with rotor-synchronized sampling of the indirect dimension and a recycle delay of 4 s. The hard pulses were optimized separately and a selective soft pulse (90°) was determined from ^{27}Al nutation experiments.

Reference

1. S. Ghose, *Acta Crystallogr.*, 1964, **17**, 1051-1057.
2. K. Momma and F. Izumi, *J. Appl. Crystallogr.*, 2011, **44**, 1272-1276.
3. C. Hobbs, C. Downing, S. Jaskaniec and V. Nicolosi, *Npj 2D Mater. Appl.*, 2021, **5**, 29.
4. R. F. Egerton, P. Li and M. Malac, *Micron*, 2004, **35**, 399-409.
5. M. C. Hales and R. L. Frost, *Polyhedron*, 2007, **26**, 4955-4962.
6. W. Zabinski, *Can. Mineral.*, 1966, **8**, 649-652.
7. J. T. Kloprogge and R. L. Frost, *J. Solid State Chem.*, 1999, **146**, 506-515.
8. D. Stoilova, V. Koleva and V. Vassileva, *Spectrochim. Acta, Part A*, 2002, **58**, 2051-2059.
9. J. T. Kloprogge, D. Wharton, L. Hickey and R. L. Frost, *Am. Mineral.*, 2002, **87**, 623-629.
10. C. A. Arguello, D. L. Rousseau and S. P. S. Porto, *Phys. Rev.*, 1969, **181**, 1351.
11. R. Cuscó, E. Alarcón-Lladó, J. Ibáñez, L. Artús, J. Jiménez, B. Wang and M. J. Callahan, *Phys. Rev. B*, 2007, **75**, 165202.
12. V. Russo, M. Ghidelli, P. Gondoni, C. S. Casari and A. L. Bassi, *J. Appl. Phys.*, 2014, **115**.
13. T. M. Devine and F. Adar, in *Characterization of Materials*, 2012, 1-38.
14. T. C. Damen, S. P. S. Porto and B. Tell, *Phys. Rev.*, 1966, **142**, 570.
15. F. Adar, *Spectroscopy*, 2014, **29**, 14.
16. J.-P. Amoureux, C. Fernandez, *Solid State Nucl. Magn. Reson.*, 1998, **10**, 211–223.